

## Research Article

# Numerical Investigations on Residual Stress in Laser Penetration Welding Process of Ultrafine-Grained Steel

Dezheng Liu<sup>1</sup>, Yan Li,<sup>1</sup> Haisheng Liu<sup>1</sup>, Zhongren Wang,<sup>1</sup> and Yu Wang<sup>2</sup>

<sup>1</sup>Department of Mechanical Engineering, Hubei University of Arts and Science, Xiangyang, Hubei 441053, China

<sup>2</sup>Shanghai Institute of Applied Physics, Chinese Academy of Sciences, Shanghai 201800, China

Correspondence should be addressed to Haisheng Liu; 185669911@qq.com

Received 27 June 2018; Revised 7 November 2018; Accepted 29 November 2018; Published 26 December 2018

Academic Editor: Antonio Boccaccio

Copyright © 2018 Dezheng Liu et al. This is an open access article distributed under the Creative Commons Attribution License, which permits unrestricted use, distribution, and reproduction in any medium, provided the original work is properly cited.

Weld solidification crack prevention in the laser penetration welding process is essential for the strength of the welded component. The formation of solidification cracks can ultimately be attributed to welding residual stresses, and preventive measures should be taken during welding. In this study, the effects of residual stresses on the laser penetration welding quality of ultrafine-grained steels were investigated. A heat source model was established through the analysis of the metallurgy of the cross section of the heat-affected zone (HAZ) of ultrafine-grained AN420s-grade steel, and the chemical composition of the weld bead was obtained using an FLS980-stm Edinburgh fluorescence spectrometer. Furthermore, the constitutive coupling relation between the temperature and material flow stress was established based on the Gibbs function, and the welding residual stress was obtained by setting trace points in a finite element analysis (FEA) model based on experimental data of the weld bead cross section under different welding conditions. The results show that weld solidification cracks will form when the residual stresses exceed the material flow stresses in the weld bead, and the residual stresses can be decreased through a reasonable increase of the welding speed. The results indicate that the proposed criterion has high accuracy and can be used to predict the formation of weld solidification cracks in the laser penetration welding process.

## 1. Introduction

Laser penetration welding, which is a stable and noncontact joining process, provides high welding speeds, good flexibility (narrow weld width and large weld depth), and high accuracy in process control [1]. The laser penetration welding technology has potential uses in additive manufacturing of ultrafine-grained steels [2, 3]. However, solidification crack formation in the fusion welding process continues to be one of the major challenges in the use of laser penetration welding technology to join ultrafine-grained steels [4]. For example, the use of laser penetration welding for new structural components still requires significant amounts of engineering data to determine its effects on the mechanical properties, such as tensile strength, fatigue strength, and the generation of residual stresses [5]. During the laser penetration welding process, the heat transfer and

liquid metal flow in the molten pool affect the grain growth direction, which may affect the weld seam structure and the properties of the weld [6]. If thermomechanical strains caused by the time-dependent temperature distribution during welding and material-specific shrinkage during the liquid- or solid-phase transition cannot be compensated for by the ductility of the weld metal or by reflow of the melt, solidification cracks will appear [7]. Furthermore, the residual stress caused by the changes in the chemical composition and the heating and cooling rates during the welding process can aggravate the initiation and growth of solidification cracks [8]. Measured residual stress data can be used for fracture analysis, safety design, and strength evaluations. However, it is difficult to experimentally measure the evolution of residual stress and solidification cracks due to the strong interference from the arc light, the rapid change in temperature, and the phase transition [5].

Thus, numerical simulations can provide valuable information to understand the laser penetration welding process of ultrafine-grained steels.

Numerical simulation methods can use multiple physics models to describe the complex physical phenomena in the molten pool [9, 10]. Many of the studies on the susceptibility to solidification cracking during the welding process using thermomechanical modelling focused on the resulting deformation and residual stresses. Frewin and Scott [11] presented a three-dimensional (3D) finite element (FE) model of the heat flow during pulsed laser beam welding. They also investigated the transient temperature profiles, dimensions of fusion, and heat-affected zone (HAZ) by incorporating temperature-dependent thermophysical properties and experimentally measured beam profiles. Shibahara et al. [12] developed a temperature-dependent interface element technique to analyze solidification cracking for mild steels. They suggested that this technique could be used to predict solidification cracks with a high accuracy. Volpp and Vollertsen [13, 14] presented an analytical method to quickly calculate the keyhole dynamics for different spatial laser intensity distributions during laser deep penetration welding. They concluded that a top hat intensity distribution led to higher maximum frequencies of the keyhole oscillations compared to a Gaussian beam profile. Dong et al. [15] indicated that the prediction of solidification cracking could be obtained by comparing the crack driving force and resistance curves. Fadaei and Mokhtari [16] presented an FE simulation and experimental measurements of the residual stresses in repair butt welds using the Goldak double-ellipsoid heat source model.

However, most recent studies on residual stresses in the laser penetration welding process were limited to numerical simulations of the evolution of temperature and residual stress fields and rarely involved the accurate modelling and analysis of the effects of transient residual and material flow stresses for weld solidification cracking.

The objective of this study was threefold. First, a heat source model was established through the analysis of the metallography of the cross section of the weld bead of ultrafine-grained AN420s-grade steel, and the chemical composition of the weld bead was measured using an FLS980-stm Edinburgh fluorescence spectrometer. Second, the constitutive coupling relation between temperature and material flow stress in the molten pool was derived. The Gibbs interface thermodynamic method and the Sente Software JMatPro were used in the derivation of the constitutive coupling relation. Third, an FE model of the molten pool was established based on the experimental data of the weld bead cross section under two different welding conditions, and four trace points were used to calculate the residual stresses in different positions of the molten pool. Emphasis was placed on the accuracy of predicting solidification cracking using the proposed criterion. Finally, a comparison between the predicted results and experimental data is given.

## 2. Materials and Methods

**2.1. Heat Source Model and Chemical Composition in Weld Bead.** The material used in the laser penetration welding was ultrafine-grained AN420s-grade steel in the form of a thick plate formed by pressure welding. Due to the dramatic changes in temperature and stress fields, the choice of a heat source model for laser welding should consider the influence of the stability of keyholes and molten pool formation [17]. Sun et al. [18] studied a new type of heat source model for laser deep welding. They suggested the use of a combined heat source model comprising a 3D cone heat source model and Gaussian surface heat source. This model exhibits Gaussian decay of the heat source radius on the surface and an exponential increase in the power density of the heat source with depth, which captures the penetration laser welding screw shape structure observed in actual welding experiments. Hence, a compound [18] cone and Gaussian surface heat source model was adopted in this work. The Gaussian surface heat source controls the surface of the molten pool and the head of the weld bead, and it can capture the effect of fluid agitation at the opening in the molten pool. The cone heat source controls the heat transfer of the liquid in deep layers and the cone body of the weld bead, and it can capture the behavior of a keyhole caused by the beam flow mining. In this compound heat source model, the power of the laser welding machine [19] can be expressed as follows:

$$\begin{aligned} P_t &= W_s + W_v + P_l, \\ W_s &= \iint \rho_m \cdot e^{-ar^2/\sigma^2} ds, \\ W_v &= \iiint R_m e^{-br^2/r_0^2} \cdot \frac{mz + r_0}{r_0} dv, \end{aligned} \quad (1)$$

where  $P_t$  is the power of the laser welding machine,  $W_s$  is the power of the surface heat source,  $W_v$  is the power of the volume heat source,  $P_l$  is the power loss caused by the reflection of the workpiece surface,  $\rho_m$  is the density of the heat flux of the surface heat source,  $R_m$  is the density of the heat flux of the volume heat source,  $\sigma$  is the heat flux distribution parameter,  $a$  is the heat flux concentration coefficient,  $b$  is the endogenous heat concentration coefficient,  $r$  is the diameter of the cone,  $r_0$  is the effective diameter of the cone,  $m$  is the coefficient of the cone shape, and  $z$  is the depth of the cone. The schematic diagram of the compound heat source model is illustrated in Figure 1.

In this heat source model, the governing equation of thermal conduction [20] can be expressed as follows:

$$\rho c \frac{\partial T}{\partial t} = k \frac{\partial^2 T}{\partial \Delta^2} + q, \quad (2)$$

where  $q$  is the intensity of the laser heating source,  $T$  is the temperature,  $t$  is the time,  $\Delta$  is the point spatial vector ( $x, y, z$ ), and  $\rho, c$ , and  $k$  are the density, specific heat, and thermal conductivity, respectively.

The HAZ in the ultrafine-grained steel was a major concern in many studies [21, 22]. In the HAZ, the microstructure of the ultrafine-grained steel undergoes severe

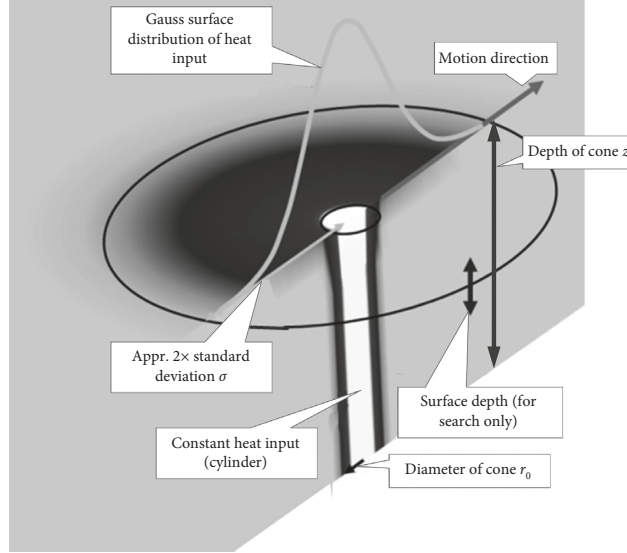


FIGURE 1: The compound heat source model.

transformations due to the influence of the welding thermal cycle, and the structure of the overheated zone changes significantly under the influence of the welding heat [21]. To investigate the microstructure and mechanical properties of the ultrafine-grained steel under laser penetration welding, the metallography of the cross section of the weld bead should be studied. The samples of ultrafine-grained steel were provided by Angang Steel Company Limited. The mechanical properties of the plate of AN420s-grade steel with dimensions of 60 mm × 30 mm × 8 mm were obtained through an experimental tension test using a SUNS UTM5000 electronic tensile testing machine under an ambient temperature of about 0°C. The mechanical properties of the AN420s-grade steel plate are shown in Table 1, where  $\sigma_s$  is the yield strength,  $\sigma_b$  is the tensile strength, and  $\delta_s$  is the extensibility.

In this study, an IPG-YSL-10000 fiber laser welder with a minimum spot diameter of 0.72 mm and an argon gas flow rate of 15 L/min were used to weld the samples. The chemical composition of the weld bead was determined using an FLS980-stm Edinburgh fluorescence spectrometer and an Olympus GX71 metallographic microscope (Figure 2). The instruments used in this study are shown in Figure 2.

**2.2. Constitutive Coupling Relation.** Residual stresses introduced in the weld bead are a consequence of incompatible thermal strains caused by heating and cooling cycles during the laser penetration welding process, and the solidification cracks can ultimately be attributed to the welding residual stresses [5]. There is a stage between the start and end of solidification where the material exhibits brittle behavior, even though the material is ductile. The end of solidification in the molten pool occurs at the temperature where all the material is solidified, which may be below the temperature where the body exhibits solid behavior macroscopically [9]. Thus, the investigation of the effects of the stress and temperature fields on the mechanical properties of the weld bead

was significant in this study. The Gibbs interface thermodynamic method [23] was adopted to establish the constitutive coupling relation between the temperature and material flow stress. The basic equation for the Gibbs energy of a multicomponent solution phase can be expressed as follows:

$$G_m = \sum_i x_i G_i^0 + RT \sum_i x_i \ln x_i + \sum_i \sum_{j>i} x_i x_j \sum_V \Omega_V (x_i - x_j)^V, \quad (3)$$

where  $\sum_i x_i G_i^0$  is the Gibbs energy of the pure components,  $RT \sum_i x_i \ln x_i$  is the ideal entropy, and  $\sum_i \sum_{j>i} x_i x_j \sum_V \Omega_V (x_i - x_j)^V$  accounts for pairwise interactions of the species. According to the Gibbs interface thermodynamic method [23], the equilibrium pressure of the system is achieved when the Gibbs free energy attains a minimum. Solute mass fraction in the solid can be expressed as follows:

$$\tau(x, T) = \frac{1}{\beta 2^{N/8} D \Delta T^q} \int_0^x \frac{dx}{x^{(2(1-x))/3} (1-x)^{(2x)/3}}, \quad (4)$$

where  $\tau$  is the solute mass fraction in the solid for different amounts of undercooling,  $\beta$  is an empirical coefficient,  $N$  is the size of a grain,  $D$  is an effective diffusion coefficient,  $\Delta T$  is the undercooling,  $q$  is an exponent that depends on the effective diffusion mechanism, and  $x$  is the fraction transformed. Based on equations (2)–(4) and the data in Table 2, the phase transition diagram of the weld bead can be calculated using JMatPro using  $N = 9$  scale by ASTM (American Society of Testing Materials).

The relationship between the stress and strain can be determined by the yield strength, hardening exponent, and reference strain [23, 24] as follows:

$$\sigma = \frac{\sigma_{0.2}}{\varepsilon_0^n} \cdot \varepsilon^n, \quad (5)$$

where  $\sigma_{0.2}$  is the yield strength,  $n$  is the hardening exponent, and  $\varepsilon_0$  is a reference strain. Using equation (5) and Figure 3,

TABLE 1: Mechanical properties of AN420s-grade steel plate.

Steel grade	Thickness (mm)	$\sigma_s$ (MPa)	$\sigma_b$ (MPa)	$\delta_s$ (%)	Remarks
AN420s	8 mm	950	1080	12	Transverse
		940	1050	12	Longitudinal
		945	1025	13	45°

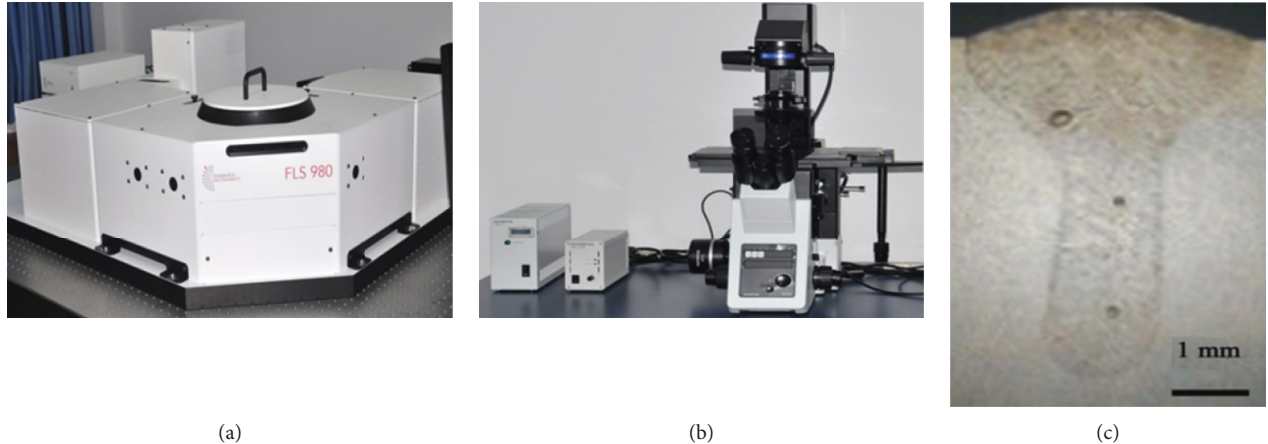


FIGURE 2: The instruments used for the analysis of the chemical composition of the weld bead. (a) FLS980-stm Edinburgh fluorescence spectrometer. (b) Metallographic microscope. (c) The cross section of the weld bead.

TABLE 2: Chemical compositions of the weld bead (wt.%).

Al	C	Fe	Mn	Nb	P	S	Si	Ti	V
0.015	0.11	97.062	1.71	0.087	0.22	0.016	0.46	0.15	0.17

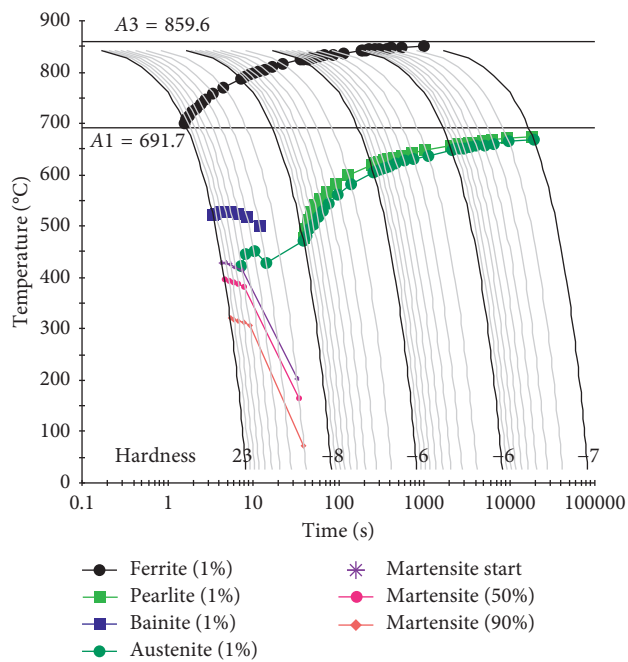


FIGURE 3: Phase transition diagram of the weld bead.

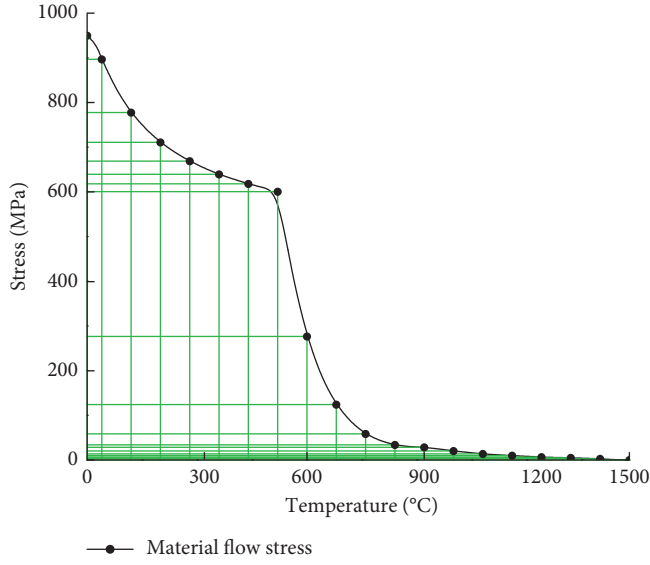


FIGURE 4: Material flow stress vs. temperature.

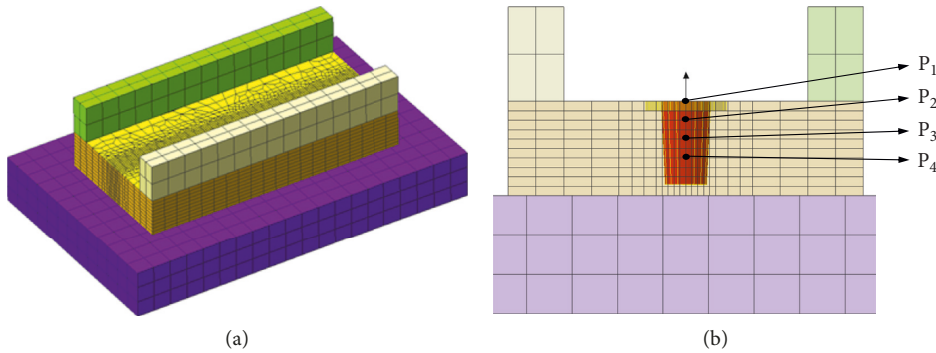


FIGURE 5: The FEA model: (a) the welding model (from top to bottom: two clamps, the welding plate, and the support plate) and (b) trace points.

TABLE 3: Input data for the FEA model.

Input data	Welding plate	Clamp	Support plate
Element size	Weld bead: 0.5 mm; base metal: 1.5 mm	2.5 mm	3 mm
Clamping force (kN)	0.3	0.3	0.3
Heat exchange coefficient	Air heat exchange coefficient: 20 W/(m <sup>2</sup> .K); weldment heat exchange coefficient: 1000W/(m <sup>2</sup> .K)		

a constitutive relation between the temperature and material flow stress can be obtained using JMatPro.

Figure 4 shows the material flow stress of ultrafine-grained AN420s-grade steel at different temperatures between the solidus and liquidus temperatures. A softening phenomenon occurs at a temperature above 500°C, and liquefaction of the material occurs at a temperature of about 1455°C, at which point the metallic state in the molten pool can be regarded as liquid. The material flow stress dramatically decreases from 610 MPa to about 50 MPa at a temperature above 500°C. The region beneath the material flow stress curve in Figure 4 can be considered a safety zone in which cracks will not form.

**2.3. FEA Model.** The finite element analysis (FEA) model of the ultrafine-grained AN420s-grade steel in the form of a vehicle component with a joint fabricated by pressure welding was created using the HyperWorks software. Subsequently, the FEA model was imported into the Simufact Welding software to analyze the laser penetration welding process. Two different welding conditions were used in this investigation. The FEA model is shown in Figure 5, the input data for the FEA model are shown in Table 3, and the welding conditions are shown in Table 4.

As shown in Figure 5(a), the total number of elements was 20040, and the ambient temperature was 20°C. To investigate the changes in the temperatures and stresses in the molten pool,

TABLE 4: The welding conditions.

Welding parameters	Power (kW)	Speed (mm/s)	Holding force (kN)	Defocusing distance (mm)
1 <sup>st</sup> condition	5.0	10.0	0.3	3
2 <sup>nd</sup> condition	5.0	20.0	0.3	3

four trace points were assigned. As shown in Figure 5(b), the trace points  $P_1$ ,  $P_2$ ,  $P_3$ , and  $P_4$  were set to collect the residual stress and temperature information in the molten pool.

The characteristics of the laser welding heat source were the local concentration and the instantaneous and heterogeneous temperature field, and an accurate heat source model can improve the accuracy of the FE simulation results [25]. A compound heat source model comprising a cone heat source and Gaussian surface heat source was adopted in this study, and the accurate heat source model was obtained through careful collation from the surface to the root of the weld between the FEA model and the cross section of the weld bead. The heat source model collation is shown in Figure 6, and the error between the simulated and actual molten pools is shown in Table 5.

### 3. Results and Discussion

**3.1. Simulated Results under the 1<sup>st</sup> Weld Operating Condition.** The effects of the welding process parameters, including the laser power, welding speed, holding force, and defocusing distance, were studied. For the 1<sup>st</sup> welding condition, the parameters were a laser power of 5.0 kW, a weld speed of 10.0 mm/s, a holding force of 0.3 kN, and a defocusing distance of 3.0 mm. Nonuniform thermal expansion and contraction due to different temperatures during the heating and cooling sequence of the welding process resulted in tensile and compressive residual stress fields in and near the weld region [26]. Figure 7 shows the temperature evolution at the trace points in the molten pool. Figures 8(a)–8(c) show the residual stresses at the trace points at different times.

As shown in Figure 7, the temperature varied with time at the four trace points. The temperature in the molten pool increased dramatically from 20°C to a maximum temperature above 1570°C in a short period of 0.5 s, after which the temperature decreased during the cooling process. As shown in Figure 8, the residual stresses varied with time at the four trace points, and the residual stress curves can be divided into four stages: (1) the metal melted, and the stress value was below 3 MPa; (2) the metal solidified, and the stress value was below 200 MPa; (3) the molten pool began to cool, and the maximum stress occurred at about 7 s; and (4) the stress fluctuated about a certain value and finally reached a steady state. The residual stresses at the four trace points eventually stabilized to constant values, and the steady-state values are shown in Table 6.

According to Table 4, the steady-state residual stress values at the trace points were in the following order:  $P_2 > P_3 > P_1 > P_4$ . Under the 1<sup>st</sup> welding condition, the highest residual stress occurred in the middle of the welding plate.

**3.2. Simulated Results under the 2<sup>nd</sup> Weld Operating Condition.** For the 2<sup>nd</sup> welding condition, the parameters

were a laser power of 5.0 kW, a weld speed of 20.0 mm/s, a holding force of 0.3 kN, and a defocusing distance of 3.0 mm. Figure 9 shows the temperature evolution at the trace points in the molten pool. Figures 10(a)–10(c) show the transient residual stresses at the trace points at different times.

As shown in Figure 9, the temperature varied with time at the four trace points. Compared to the 1<sup>st</sup> welding condition, the highest temperature in the molten pool under the 2<sup>nd</sup> welding condition increased by about 5% from 1530 to 1600°C. As shown in Figure 10, the residual stresses varied with time at the four trace points, and the residual stress curve can be divided into four stages: (1) the metal melted, and the stress value was below 3 MPa; (2) the metal solidified, and the stress value was below 200 MPa; (3) the molten pool began to cool, and the maximum stress occurred at about 6 s; and (4) the stress fluctuated about a certain value and finally reached a steady state. The residual stresses at the four trace points eventually stabilized to constant values, and the steady-state values are shown in Table 7.

According to Table 4, the steady-state residual stress values at the trace points were in the following order:  $P_2 > P_1 > P_4 > P_3$ . Under the 2<sup>nd</sup> welding condition, the highest residual stress occurred in the middle of the welding plate.

**3.3. Discussion.** The results from the two different sets of welding parameters indicated that the highest residual stresses occurred in the middle of the welding plate, which corresponds to the trace point  $P_2$ . However, the highest value of residual stress under the 2<sup>nd</sup> welding condition was significantly less than that under the 1<sup>st</sup> welding condition. When the welding speed increased and the weld pool geometry became tapered, the solidification cracks will be more concentrated and in positions near the centerline. Under this condition, the liquid flow rate was high and the rate of volume change was low. To investigate the effects of the residual stress on the solidification cracking behavior, a comparison between the experimental results and the predicted stress distributions under the two operating conditions is shown in Figure 10. The metallography of the cross sections of the weld beads under the two welding conditions was obtained using the Olympus GX71 metallographic microscope.

Figure 11 shows the cracks observed in the molten pool under the 1<sup>st</sup> welding condition. Upon increasing the weld speed from 10.0 to 20.0 mm/s for the 2<sup>nd</sup> welding condition, no cracks formed. Sheikhi et al. [27] reported that a low solidification rate and a small vulnerable zone were ideal for producing a weld without any cracks. Figures 11(c) and 11(d) show that the stresses in the molten pool under the 1<sup>st</sup> welding condition were higher than those under the 2<sup>nd</sup> welding condition, and high stresses in the molten pool increased the liquid flow. The constitutive coupling relation

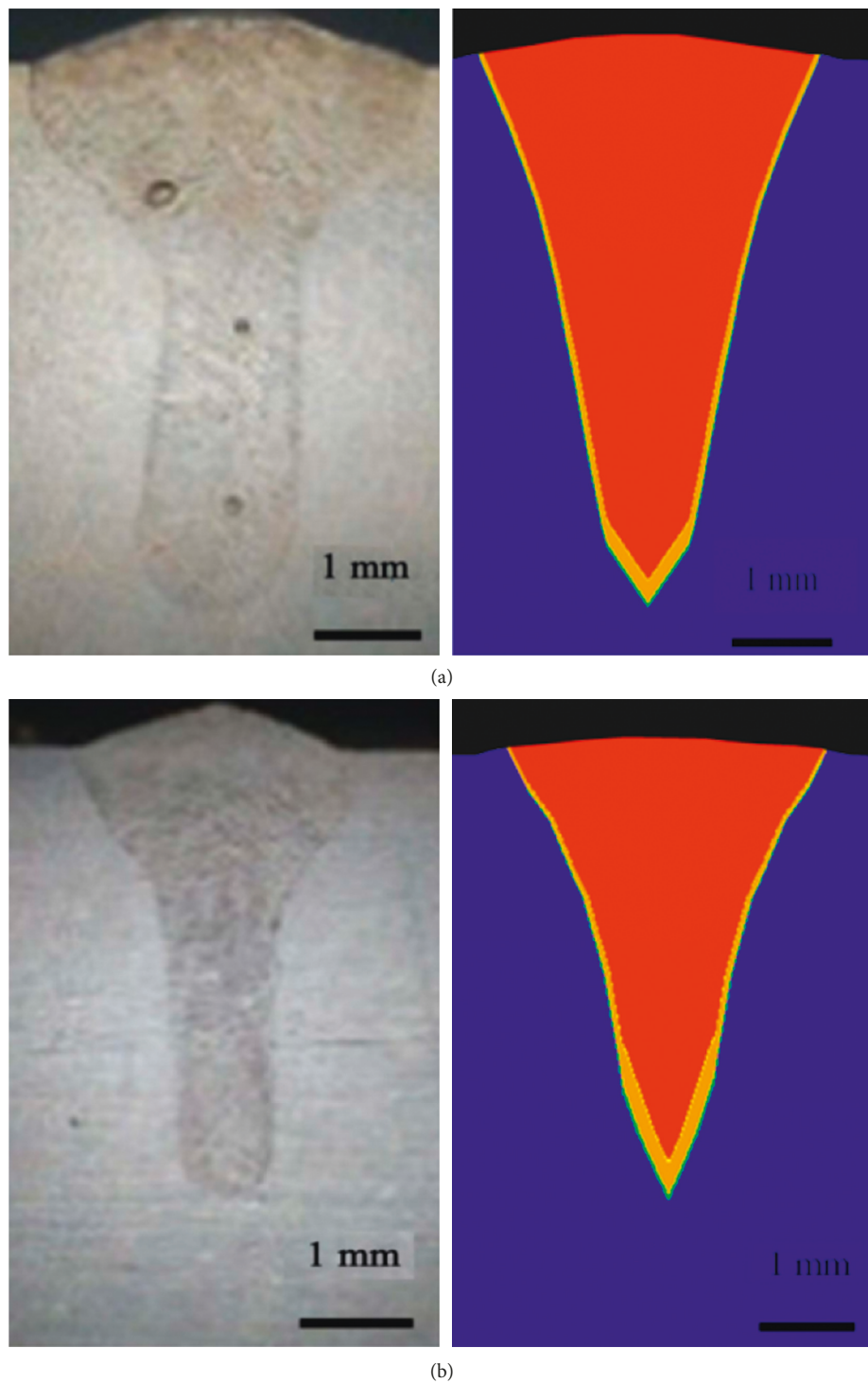


FIGURE 6: The heat source model collation: the collation under the (a) 1<sup>st</sup> and (b) 2<sup>nd</sup> welding conditions.

TABLE 5: The percentage error between the simulated and actual molten pools.

	Weld width (mm)		Weld depth (mm)		Maximum percentage error (%)
	Experimental data	FEA model	Experimental data	FEA model	
1 <sup>st</sup> condition	4.0	4.068	5.4	5.387	0.2
2 <sup>nd</sup> condition	3.5	3.523	4.2	4.186	0.3

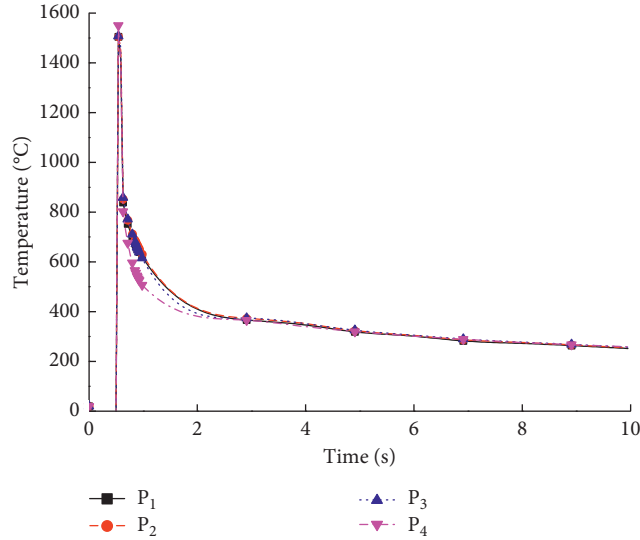


FIGURE 7: The temperature evolution at the trace points (1<sup>st</sup> welding condition).

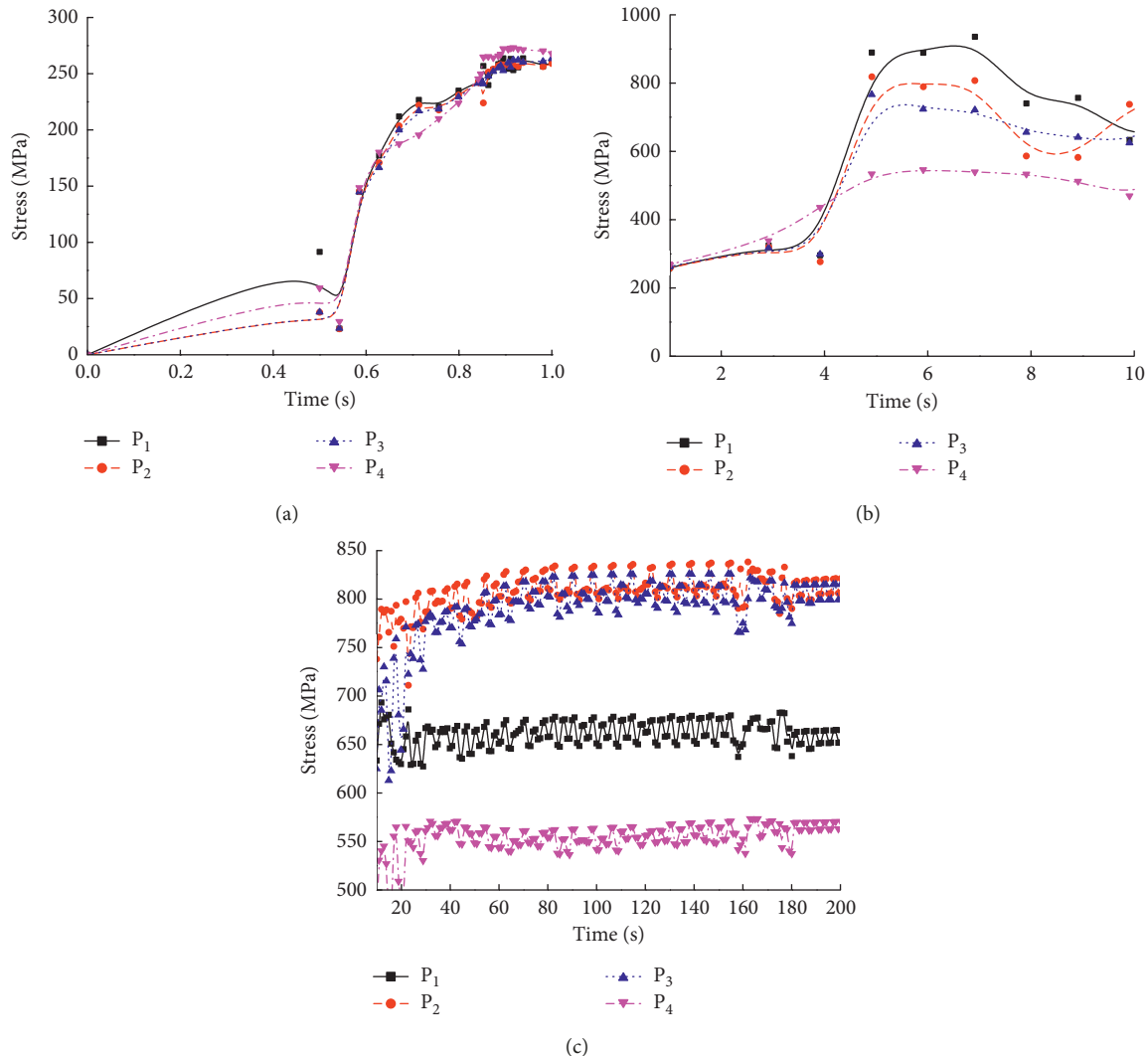


FIGURE 8: The residual stresses at the trace points at different times (1<sup>st</sup> welding condition): (a) 0–1 s; (b) 1–10 s; (c) 10–200 s.

TABLE 6: Steady-state residual stresses at the trace points.

Trace point	P <sub>1</sub>	P <sub>2</sub>	P <sub>3</sub>	P <sub>4</sub>
Steady-state value of stress (MPa)	650	820	800	570

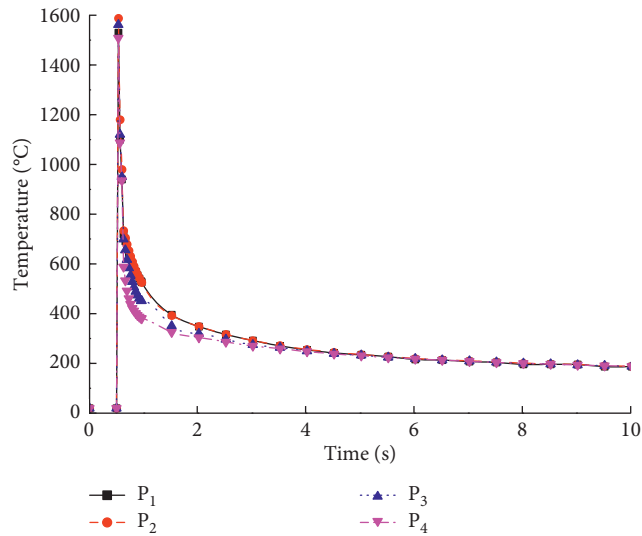
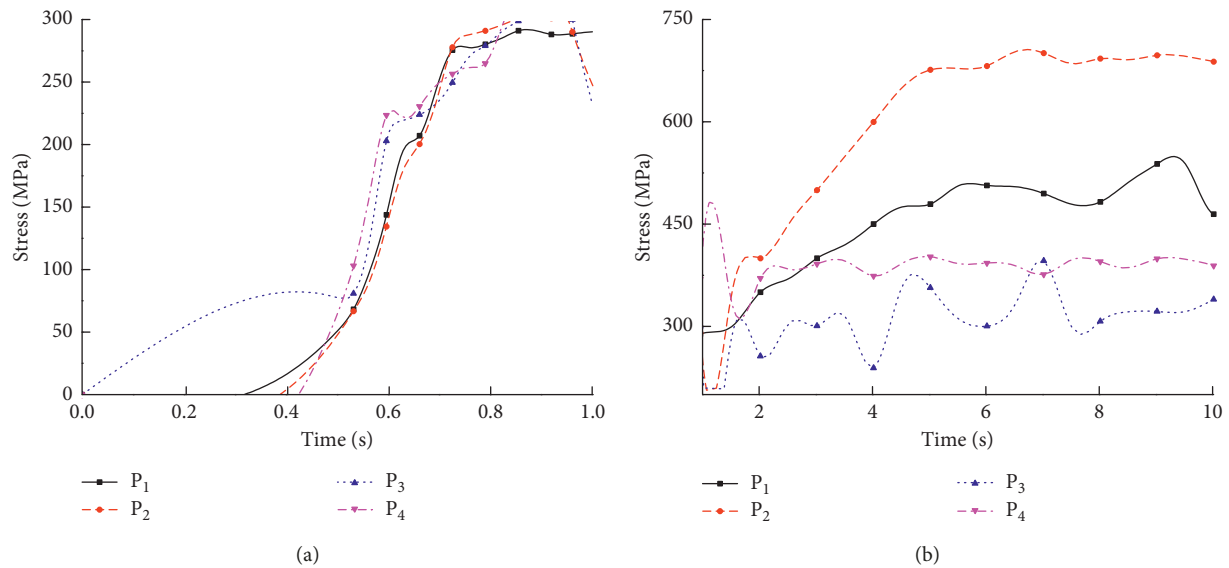
FIGURE 9: The temperature evolution at the trace points (2<sup>nd</sup> welding condition).

FIGURE 10: Continued.

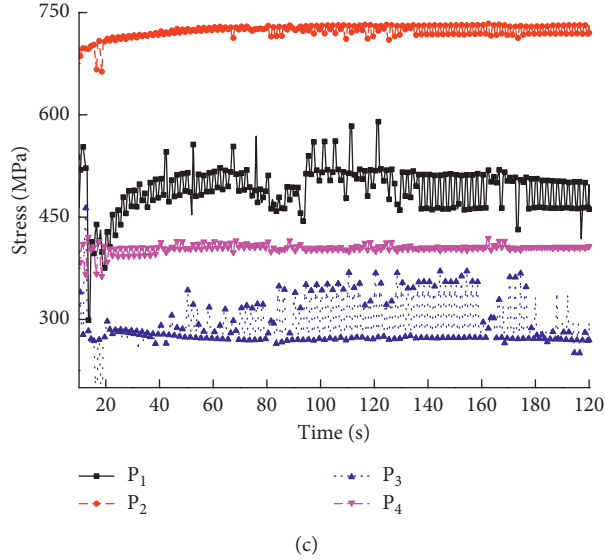


FIGURE 10: The residual stresses at the trace points at different times (2<sup>nd</sup> welding condition): (a) 0–1 s; (b) 1–10 s; (c) 10–200 s.

TABLE 7: Steady-state residual stresses at the trace points.

Trace point	P <sub>1</sub>	P <sub>2</sub>	P <sub>3</sub>	P <sub>4</sub>
Steady-state value of stress (MPa)	475	720	280	410

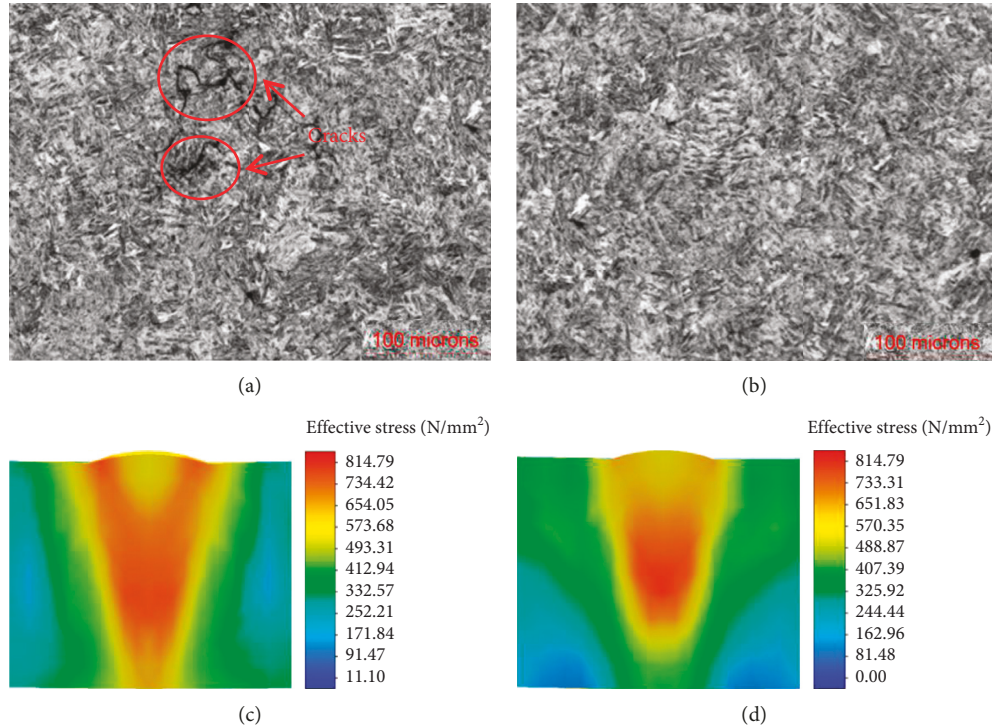


FIGURE 11: Comparison between the measured and the simulated results: the cross section of the weld bead under the (a) 1<sup>st</sup> and (b) 2<sup>nd</sup> welding conditions; the stress distributions under the (c) 1<sup>st</sup> and (d) 2<sup>nd</sup> welding conditions.

between the temperature and material flow stress is shown in Figure 4. The residual stresses at the trace point P<sub>2</sub> at different temperatures were extracted and compared to the material flow stress curve.

Figure 12 shows a comparison of the highest residual stress curve under the two welding conditions and the material flow stress curve. Based on Figures 11 and 12, the effects of residual stress on the laser penetration welding

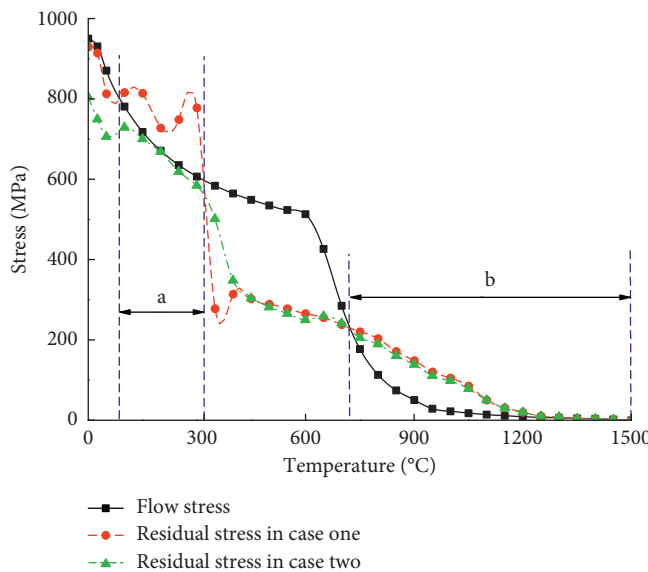


FIGURE 12: Comparison between the residual stress and the material flow stress.

process of ultrafine-grained steel can summarized as follows:

- (1) In the temperature range of interval *b*, the residual stresses under the two different welding conditions were higher than the material flow stresses. The weld bead was not completely solidified, and the state of the molten pool was a mixture of solid and liquid. The liquid still available between the solid cells was continuous and could move easily, since the solid cells have not yet coalesced, and compensates for the deformation induced by shrinkage and thermal stresses. Thus, for temperatures in the interval *b*, cracks will occur.
- (2) In the temperature range of interval *a*, the weld bead was completely solidified, and the solid cells coalesced. The residual stresses under the 1<sup>st</sup> welding condition were higher than the material flow stresses, and cracks will form in this case. The residual stresses under the 2<sup>nd</sup> welding condition were lower than the material flow stresses, and cracks will not form in this case. These conclusions are in good agreement with the experimental results.
- (3) The residual stresses under the two different welding conditions were nearly equal when the temperature was above 400°C. The residual stresses under the 1<sup>st</sup> welding condition quickly exceeded the residual stresses under the 2<sup>nd</sup> welding condition, indicating that cracks will form during the cooling process of the molten pool. This also explains why a reasonable increase of the welding speed can prevent solidification cracks in the laser penetration welding process of ultrafine-grained steel.

#### 4. Conclusions

In this study, the residual stresses in the laser penetration welding process of ultrafine-grained steel were investigated.

A constitutive coupling relation between the temperature and material flow stress in the molten pool was developed based on the Gibbs interface thermodynamic method. An FE model of the molten pool was established based on experimental data of the weld bead cross section under two different welding conditions. Lastly, a criterion for assessing the formation of solidification cracks in the laser penetration welding process was proposed. From the experimental work and modelling, the following conclusions were drawn:

- (1) At the same temperature and position in the molten pool, when the residual stress is higher than the material flow stress of ultrafine-grained steel, cracks will form in the weld bead.
- (2) A reasonable increase of the welding speed can decrease the residual stress in the molten pool and enhance the laser penetration welding quality for ultrafine-grained steel.
- (3) The proposed criterion obtained through the comparison of the residual stress and material flow stress curves of the ultrafine-grained steel can provide a new method to evaluate the formation of solidification cracks in weld beads.

#### Data Availability

The data used to support the findings of this study are available from the corresponding author upon request.

#### Conflicts of Interest

The authors declare that they have no conflicts of interest.

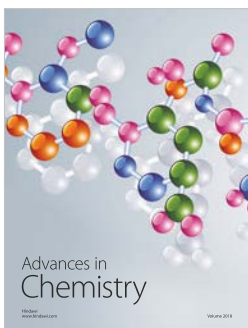
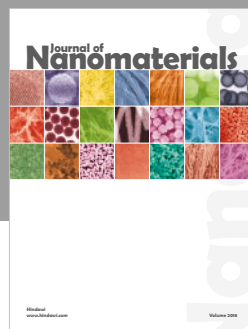
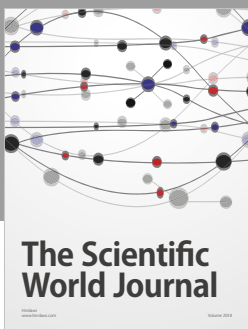
#### Acknowledgments

The authors gratefully acknowledge the use of the services and facilities of AVIC Hubei Aviation Precision Machinery Technology Co, Ltd. and Hubei Key Laboratory of Power System Design and Test for Electrical Vehicle. This research was funded by the Youth Project of Hubei Provincial Department of Education (No. Q20172603), Hubei Superior and Distinctive Discipline Group of Mechatronics and Automobiles (No. XKQ2018065), and Hubei Superior and Distinctive Discipline Group of Mechatronics and Automobiles (No. XKQ2018009).

#### References

- [1] S. Chen, D. Yang, M. Li et al., "Laser penetration welding of an overlap titanium-on-aluminum configuration," *International Journal of Advanced Manufacturing Technology*, vol. 87, no. 9–12, pp. 3069–3079, 2016.
- [2] Y. Zhang, F. Li, Z. Liang, Y. Ying, Q. Lin, and H. Wei, "Correlation analysis of penetration based on keyhole and plasma plume in laser welding," *Journal of Materials Processing Technology*, vol. 256, pp. 1–12, 2018.
- [3] C. C. Zhao, W. N. Li, and Z. B. Liu, "Laser welding of ultrafine grained steel ss400," *Journal of Iron and Steel Research (International)*, vol. 10, no. 3, pp. 32–36, 2003.
- [4] H. L. Wei, J. J. Blecher, T. A. Palmer, and T. Debroy, "Fusion zone microstructure and geometry in complete-joint-

- penetration laser-arc hybrid welding of low-alloy steel," *Welding Journal*, vol. 94, no. 4, pp. 135–144, 2015.
- [5] R. A. Sindhu, M. K. Park, S. J. Lee, and K. D. Lee, "Effects of residual stresses on the static and fatigue strength of laser-welded lap joints with different welding speeds," *International Journal of Automotive Technology*, vol. 11, no. 6, pp. 857–863, 2010.
- [6] L.-J. Zhang, G.-F. Zhang, X.-Y. Bai, J. Ning, and X.-J. Zhang, "Effect of the process parameters on the three-dimensional shape of molten pool during full-penetration laser welding process," *The International Journal of Advanced Manufacturing Technology*, vol. 86, no. 5–8, pp. 1273–1286, 2016.
- [7] E.-J. Chun, H. Baba, K. Nishimoto, and K. Saida, "Development of laser beam welding transverse-varestraint test for assessment of solidification cracking susceptibility in laser welds," *Metals and Materials International*, vol. 21, no. 3, pp. 543–553, 2015.
- [8] C. Lee, H. Park, J. Yoo, C. Lee, W. Woo, and S. Park, "Residual stress and crack initiation in laser clad composite layer with co-based alloy and wc + nicr," *Applied Surface Science*, vol. 345, pp. 286–294, 2015.
- [9] X. Li, F. Lu, H. Cui, X. Tang, and Y. Wu, "Numerical modeling on the formation process of keyhole-induced porosity for laser welding steel with t-joint," *The International Journal of Advanced Manufacturing Technology*, vol. 72, no. 1–4, pp. 241–254, 2014.
- [10] G. Pastras, A. Fysikopoulos, C. Giannoulis, and G. Chryssolouris, "A numerical approach to modeling key-hole laser welding," *The International Journal of Advanced Manufacturing Technology*, vol. 78, no. 5–8, pp. 723–736, 2014.
- [11] M. R. Frewin and D. A. Scott, "Finite element model of pulsed laser welding," *Welding Research Supplement*, vol. 78, pp. 15–22, 1999.
- [12] M. Shibara, H. Serizawa, and H. Murakawa, "Finite element method for hot cracking using temperature dependent interface element (Report II)," *Trans JWRI*, vol. 29, no. 1, pp. 59–64, 2000.
- [13] J. Volpp, "Investigation on the influence of different laser beam intensity distributions on keyhole geometry during laser welding," *Physics Procedia*, vol. 39, no. 9, pp. 17–26, 2012.
- [14] J. Volpp and F. Vollertsen, "Modeling keyhole oscillations during laser deep penetration welding at different spatial laser intensity distributions," *Production Engineering*, vol. 9, no. 2, pp. 167–178, 2014.
- [15] Z. Dong, M. A. Rui, W. Yong, X. Zhan, and Y. Wei, "Post-data treatment design of software package for three dimensional simulation and prediction of weld solidification cracks," *Transactions of the China Welding Institution*, vol. 32, no. 3, pp. 17–20, 2011.
- [16] A. Fadaei and H. Mokhtari, "Finite element modeling and experimental study of residual stresses in repair butt weld of ST-37 plates," *Iranian Journal of Science & Technology Transactions of Mechanical Engineering*, vol. 39, pp. 291–307, 2015.
- [17] L. Zhang, J. Zhang, G. Zhang, W. Bo, and S. Gong, "An investigation on the effects of side assisting gas flow and metallic vapour jet on the stability of keyhole and molten pool during laser full-penetration welding," *Journal of Physics D: Applied Physics*, vol. 44, no. 13, pp. 135–201, 2011.
- [18] Q. D. Sun, L. I. Meng-Sheng, and R. W. Song, "Research on a new type of heat source model on laser deep welding," *Welding Technology*, vol. 39, no. 12, pp. 11–14, 2010.
- [19] G. L. Qin, X. B. Qi, Y. B. Yang, X. Y. Wang, and S. Y. Lin, "Acquisition and processing of coaxial image of molten pool and keyhole in nd:yag laser welding with high power," *China Welding*, vol. 13, no. 1, pp. 51–55, 2004.
- [20] C. Lampa, A. F. H. Kaplan, J. Powell, and C. Magnusson, "An analytical thermodynamic model of laser welding," *Journal of Physics D: Applied Physics*, vol. 30, no. 9, pp. 1293–1299, 1999.
- [21] H. Halfa, "Recent trends in producing ultrafine grained steels," *Journal of Minerals and Materials Characterization and Engineering*, vol. 2, no. 5, pp. 428–469, 2014.
- [22] P. Layus, P. Kah, A. Zisman, M. Pirinen, and S. Golosienko, "Recrystallization-based formation of uniform fine-grained austenite structure before polymorphic transition in high-strength steels for arctic applications," *International Journal of Mechanical & Materials Engineering*, vol. 11, no. 1, pp. 1–7, 2016.
- [23] J. Gernert, A. Jäger, and R. Span, "Calculation of phase equilibria for multi-component mixtures using highly accurate helmholtz energy equations of state," *Fluid Phase Equilibria*, vol. 375, no. 31, pp. 209–218, 2014.
- [24] S. A. English and N. K. Arakere, "Effects of the strain-hardening exponent on two-parameter characterizations of surface-cracks under large-scale yielding," *International Journal of Plasticity*, vol. 27, no. 6, pp. 920–939, 2011.
- [25] A. Belitzki and M. F. Zaeh, "Accuracy of calculated component distortions using the weld pool length to calibrate the heat source," *Journal of Laser Applications*, vol. 28, no. 2, article 022424, 2016.
- [26] J. Ahn, E. He, L. Chen et al., "Fem prediction of welding residual stresses in fibre laser-welded aa 2024-t3 and comparison with experimental measurement," *International Journal of Advanced Manufacturing Technology*, vol. 95, no. 5, pp. 1–21, 2018.
- [27] M. Sheikhi, F. Malek Ghaini, and H. Assadi, "Prediction of solidification cracking in pulsed laser welding of 2024 aluminum alloy," *Acta Materialia*, vol. 82, pp. 491–502, 2015.



Hindawi

Submit your manuscripts at  
[www.hindawi.com](http://www.hindawi.com)

